Journal of Controlled Release 337 (2021) 285–295

Contents lists available at ScienceDirect

Journal of Controlled Release

journal homepage: www.elsevier.com/locate/jconrel

Acoustic Cluster Therapy (ACT®) enhances accumulation of polymeric micelles in the murine brain

Marieke Olsman [a,1], Melina Mühlenpfordt [a,*,1], Emma Bøe Olsen [a], Sverre H. Torp [b,c], Spiros Kotopoulis [d,e], Cristianne J.F. Rijcken [f], Qizhi Hu [f], Marielle Thewissen [f], Sofie Snipstad [a,g], Catharina de Lange Davies [a]

[a] Department of Physics, Norwegian University of Science and Technology, Trondheim, Norway
[b] Department of Clinical and Molecular Medicine, Norwegian University of Science and Technology, Trondheim, Norway
[c] Department of Pathology, St. Olavs Hospital, Trondheim University Hospital, Trondheim, Norway
[d] National Centre for Ultrasound in Gastroenterology, Haukeland University Hospital, Bergen, Norway
[e] Exact Therapeutics, Oslo, Norway
[f] Cristal Therapeutics, Maastricht, the Netherlands
[g] Cancer Clinic, St. Olavs Hospital, Trondheim, Norway

ARTICLE INFO

Keywords:
Therapeutic ultrasound
Blood-brain barrier
CCPM
ACT®
Nanomedicine
Dual frequency transducer

ABSTRACT

The restrictive nature of the blood-brain barrier (BBB) prevents efficient treatment of many brain diseases. Focused ultrasound in combination with microbubbles has shown to safely and transiently increase BBB permeability. Here, the potential of Acoustic Cluster Therapy (ACT®), a microbubble platform specifically engineered for theranostic purposes, to increase the permeability of the BBB and improve accumulation of IRDye® 800CW-PEG and core-crosslinked polymeric micelles (CCPM) in the murine brain, was studied. Contrast enhanced magnetic resonance imaging (MRI) showed increased BBB permeability in all animals after ACT®. Near infrared fluorescence (NIRF) images of excised brains 1 h post ACT® revealed an increased accumulation of the IRDye® 800CW-PEG (5.2-fold) and CCPM (3.7-fold) in ACT®-treated brains compared to control brains, which was retained up to 24 h post ACT®. Confocal laser scanning microscopy (CLSM) showed improved extravasation and penetration of CCPM into the brain parenchyma after ACT®. Histological examination of brain sections showed no treatment related tissue damage. This study demonstrated that ACT® increases the permeability of the BBB and enhances accumulation of macromolecules and clinically relevant nanoparticles to the brain, taking a principal step in enabling improved treatment of various brain diseases.

1. Introduction

A functional blood-brain barrier (BBB) is crucial for neural function and protection against toxins and pathogens. The BBB, formed of specialized cerebral endothelial cells, pericytes, astrocytes and immune cells, tightly regulates paracellular and transcellular transport of molecules to the brain. Due to its highly restrictive nature, only small, hydrophilic molecules (<400–500 Da) can pass, excluding most drug candidates to efficiently treat brain diseases [1,2]. Different strategies ranging from chemical, biological to physical stimuli have been employed to circumvent the BBB, but often resulted in insufficient localization, low therapeutic efficacy, damage to healthy tissue or adverse systemic effects [3–6].

Non-invasive focused ultrasound treatment in combination with systemically injected microbubbles, has shown to safely and transiently increase the BBB permeability at the targeted site [7–15]. Most microbubbles used for ultrasound-induced increase of BBB permeability are regular ultrasound contrast agents, such as Optison™, Definity™ and SonoVue™, primarily designed and optimized for diagnostic purposes. Due to their small size (diameter 1–3 μm) diagnostic microbubbles are free flowing in the vasculature and achieve only limited contact with the vessel wall, making them less optimal for therapeutic applications.

Acoustic Cluster Therapy (ACT®) provides a novel microbubble platform addressing the shortcomings of current microbubbles [16,17].

* Corresponding author.
E-mail address: melina.muhlenpfordt@ntnu.no (M. Mühlenpfordt).
[1] Shared first authorship.

https://doi.org/10.1016/j.jconrel.2021.07.019
Received 8 April 2021; Received in revised form 22 June 2021; Accepted 13 July 2021
Available online 16 July 2021
0168-3659/© 2021 The Authors. Published by Elsevier B.V. This is an open access article under the CC BY license (http://creativecommons.org/licenses/by/4.0/).

The ACT®-concept comprises an intravenous co-injection of therapeutic agents and microdroplet-microbubble clusters. Using high frequency ultrasound (≥ 2- MHz), microbubbles transfer energy to the microdroplets inducing droplet vaporization, forming large activated ACT® bubbles (20–25 μm), which transiently lodge in a small fraction of the targeted vasculature. The second ultrasound exposure at lower frequency (500 kHz) induces controlled volume oscillations of the ACT® bubbles, exerting biomechanical forces on the capillary wall and enhancing local accumulation of the co-injected therapeutic agent at the targeted site [18]. ACT® bubbles will cover larger areas within the blood vessel and stay for a prolonged time, resulting in intensified contact with the endothelium compared to conventional microbubbles [16]. No severe side effects of ACT® were observed in pre-clinical safety assessments [19]. Several pre-clinical studies in different cancer models have demonstrated the improved therapeutic efficacy when chemotherapeutic agents were combined with ACT® [20–23]. Due to the promising pre-clinical results, a first in man study (NCT04021277) assessing safety and efficacy of ACT® combined with standard of care chemotherapy is currently being conducted.

The potential of ACT® to increase the permeability of the BBB and consequent brain uptake remains largely understudied. An initial proof of principle study in healthy rats showed increased BBB permeability after ACT®, leading to increased accumulation of a small model drug [24]. These experiments were conducted with sub-optimal ultrasound frequencies, not fully exploiting the potential of ACT®.

In recent years, core-crosslinked polymeric micelles (CCPM) have emerged as promising nanomedicine to improve therapeutic performance of a range of drug candidates [25]. Particularly, a polymeric nanoparticle platform known as CriPec® enables the manufacturing of biodegradable CCPM with active pharmaceutical ingredients (API) temporarily covalently entrapped via hydrolysable linkers. Key pharmaceutical characteristics of the generated CCPM such as particle size and API release kinetics are highly customisable, enabling a wide range of applications [26]. Preclinical evaluation has shown excellent pharmacokinetics resulting in improved target tissue accumulation and efficacy for various drugs including docetaxel and dexamethasone [27,28]. CCPM with entrapped docetaxel demonstrated excellent clinical translation, since prolonged systemic circulation, improved safety profile and 4-fold enhanced tumor uptake was demonstrated in patients with advanced solid tumours [29]. However, as for most other drug nanocarriers, uptake in brain was absent due to the dense BBB impeding access. Combining ACT® with clinically relevant nanomedicine would hold great promise for treating a variety of brain disorders.

In this study, a custom-built dual frequency ultrasound transducer [30] was used for ACT® to increase BBB permeability. The extent of BBB permeability increase was evaluated with contrast-enhanced magnetic resonance imaging (MRI). Accumulation of the small model drug IRDye® 800CW-PEG and 65 nm dual fluorophore-labelled CCPM in healthy mice brains was studied using near infrared fluorescence (NIRF) imaging. Brain sections were imaged by confocal laser scanning microscopy (CLSM) to analyze the micro-distribution of CCPM or stained with haematoxylin erythrosine saffron (HES) to evaluate the safety of ACT®.

2. Material and methods

2.1. ACT® formulation

The ACT® formulation consisted of a dispersion of microbubble/microdroplet clusters and was kindly provided by EXACT Therapeutics AS (Oslo, Norway). A more detailed description of the ACT® formulation was published previously [16]. In brief, the commercially available negatively charged microbubbles Sonazoid™ (GE Healthcare AS, Oslo, Norway) are reconstituted with 2 ml of a positively charged microdroplet emulsion of 4 μl/ml perfluoromethylcyclopentane (PFMCP) stabilized with a distearoylphosphatidylcholine (DSPC) phospholipid membrane containing 3% (mol/mol) stearyl amine (SA), all dispersed in a 5 mM TRIS buffer. Once reconstituted, the formulation consists of a suspension of microbubble/microdroplet clusters with a median diameter of 4.5 μm [16].

2.2. IRDye® 800CW-PEG and CCPM

The vascular contrast agent IRDye® 800CW-PEG (25–60 kDa; LI-COR, USA) was used as a model compound (stock: 1 nmol/100 μl).

Cy7, rhodamine B-labelled CCPM were manufactured and kindly provided by Cristal Therapeutics (Cristal Therapeutics, Maastricht, The Netherlands). The near infrared fluorophore Cy7 was used to image in vivo brain accumulation of the CCPM by NIRF. Rhodamine B was used to study the microdistribution of CCPM by CLSM.

In brief, first, rhodamine B was conjugated to a fraction (6.6 mol%) of the lactate side chains of methacrylated $mPEG_{5000}$-*b*-pHPMAmLac$_n$ (n = 1 or 2) block copolymer (22 kDa) via Steglich esterification [31] to obtain rhodamine-labelled block copolymers. Next, fluorophores-labelled CCPM were manufactured essentially following the protocol reported previously [32], except that a mixture of azide-functionalised (5 mol%), rhodamine-labelled (33 mol%) and non-functionalised (62 mol%) methacrylated $mPEG_{5000}$-*b*-pHPMAmLac$_n$ (n = 1 or 2) block copolymers (22 kDa) was used to form azide-functionalised rhodamine-labelled CCPM prior to Cy7 conjugation. Analytical characterisations revealed that the obtained Cy7, rhodamine-labelled CCPM (88 mg/ml polymer, 40 μM Cy7 equiv. and 9 mM rhodamine equiv.) has a hydrodynamic size of 65 nm, with free rhodamine dye and free Cy7 label less than 1 mol% relative to that covalently attached to CCPM.

2.3. Animals

49 female albino BL6 mice, purchased at 6–8 weeks of age (Janvier labs, France), were housed in groups of five in individually ventilated cages under conditions free of specific pathogens. Cages were enriched with housing, nesting material and gnaw sticks, and were kept in a controlled environment (20–23 °C, humidity of 50–60%) at a 12-h night/day cycle. Animals had free access to food and sterile water. All experimental procedures were approved by the Norwegian Food Safety Authority.

2.4. MR-imaging

MR-imaging was performed with a 7.05 T horizontal bore magnet (Biospec 70/20 Avance III, Bruker Biospin) with an 86 mm volume resonator for RF transmission and a 4-channel phased array cryocoil for reception.

Animals were scanned pre, immediately after (post) and in some cases 24 h and 48 h post ACT®. Before each MRI scan, animals received an intravenous bolus injection of a gadolinium-based contrast agent (1.5 ml/kg, 0.5 mmol/ml, Omniscan™, GE Healthcare). BBB permeability was evaluated by detecting extravasated contrast agent with a T1 RARE sequence (Echo time (TE) 6.3 ms, repetition time (TR) 1500 ms and 4 averages). A T2 RARE sequence was acquired for detecting oedema (TE 40 ms, TR 4000 ms and 2 averages). A T1 FLASH sequence was acquired to detect haemorrhages (TE 6.5 ms, TR 30 ms, flip angle 20° and 2 averages). All sequences had a field of view of 25.6 mm × 16.0 mm, with a matrix size of 256 × 160, a slice thickness of 0.4 mm and 25 slices spaced 0.4 mm. MR acquisition parameters were set using Bruker Paravision 6.0.1.

2.5. Ultrasound set-up

An illustration of the ultrasound set-up is shown in Fig. 1. A custom-built dual frequency transducer, which utilizes the first (0.5 MHz) and fifth harmonic (2.7 MHz) [30], was mounted on top of a custom-made cone filled with degassed water. The transducer had a diameter of 42

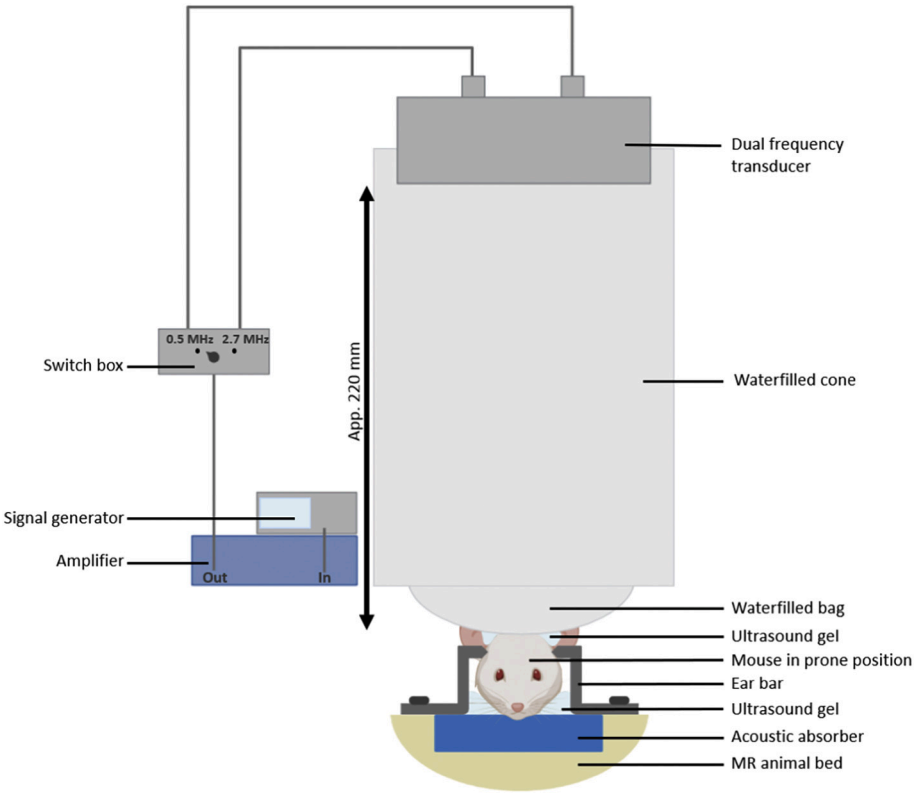

Fig. 1. Not-to-scale illustration of the ultrasound set-up used during ACT®. Nose gas mask is not shown. All connections are achieved through BNC cables. The animal is placed in prone position on the MR animal bed and the head is fixed by ear bars. The entire MR animal bed is placed in the ultrasound set-up.

mm and 220 mm away from the transducer surface, the −3 dB width of the beam profile of 0.5 MHz and 2.7 MHz were 16 and 6 mm, respectively. Signals were generated with a signal generator (33500B, Agilent Technologies, USA) and amplified with a 50 dB RF amplifier (2100 L, E&I, USA). The amplifier was connected to the switch box which contained two electrical circuits for electrical matching of both frequencies. Electrical tuning was needed to achieve efficient transfer of electrical energy to acoustic energy by the transducer. Switching between the two electrical configurations was achieved with a rotary switch [30].

The bottom of the cone was covered with an optically and acoustically transparent plastic foil (Jula Norge AS, Norway), forming a bag. The animal was positioned in prone position on top of an acoustically absorbing material (Aptflex F28, Precision Acoustics, UK), with ultrasound gel for coupling between the acoustic absorber, the animals head and the acoustically transparent foil. The head was fixed with ear bars to prevent motion artefacts during MR imaging and to prevent movement of the head when the cone was lowered until the foil was in contact with the head.

2.6. ACT®

ACT® consisted of a bolus injection of 25 μl of ACT® clusters prior to the 60 s activation ultrasound and 300 s enhancement insonation. After each injection, the catheter was flushed with 25 μl of saline. Each animal received 3 times ACT®, resulting in a total of 75 μl ACT® formulation and 18 min ultrasound.

The attenuation through the murine skull was measured to be approximately 21 ± 17% and 42 ± 21% for the 0.5 MHz and 2.7 MHz frequencies, respectively (see supplementary information). The following attenuation compensated in situ ultrasound parameters were used for each step:

- **Activation:** Frequency of 2.7 MHz, Peak negative pressure (PNP) of 0.21 MPa and corresponding mechanical index (MI) of 0.13, Peak positive pressure (PPP) of 0.41 MPa, 8 cycles pulse length, pulse repetition frequency of 1 kHz and sonication time of 60 s.
- **Enhancement:** Frequency of 0.5 MHz, PNP of 0.1 MPa and corresponding MI of 0.14, PPP of 0.09 MPa, 4 cycles pulse length, pulse repetition frequency of 1 kHz and sonication time of 300 s.

2.7. Experimental procedure – ACT®-induced delivery of the IRDye® 800CW-PEG and CCPM

The timeline of the experimental procedure is presented in Fig. 2. Animals were anaesthetized using 2% isoflurane in medical air (78%) and oxygen (20%) (Baxter, USA) after which their lateral tail vein was cannulated. Hair was removed with a hair trimmer and depilatory cream (Veet, Canada). The animals were placed in prone position on the MRI-bed and a pre-scan (Pre-MRI scan) was performed before the MRI-bed was placed in the ultrasound set-up. During MRI-imaging and ACT®, animals were anaesthetized using 1.5–2% isoflurane in medical air. Respiration rate was monitored using a pressure sensitive probe (SA instruments, USA). The body temperature was monitored by a rectal temperature probe (SA instruments, USA) and maintained at 37 °C with external heating.

Prior to ACT®, 50 μl of IRDye® 800CW-PEG (final concentration of 5 pmol/g body weight) or 50 μl of CCPM solution (final Cy7 dosage of 2 nmol Cy7 equiv. per animal) was intravenously injected. Each animal received 3 times ACT® followed by another MRI-scan (Post-MRI scan). Control animals were handled in the same way as the ACT® animals but received 3 times 25 μl saline instead of the ACT® formulation. A total of 37 animals were included in the various groups, as shown in Table 1.

To study whether an increased BBB permeability could still be detected 24 h post ACT® and to study the accumulation of both the IRDye® 800CW-PEG and CCPM at this timepoint, a subgroup of the 37

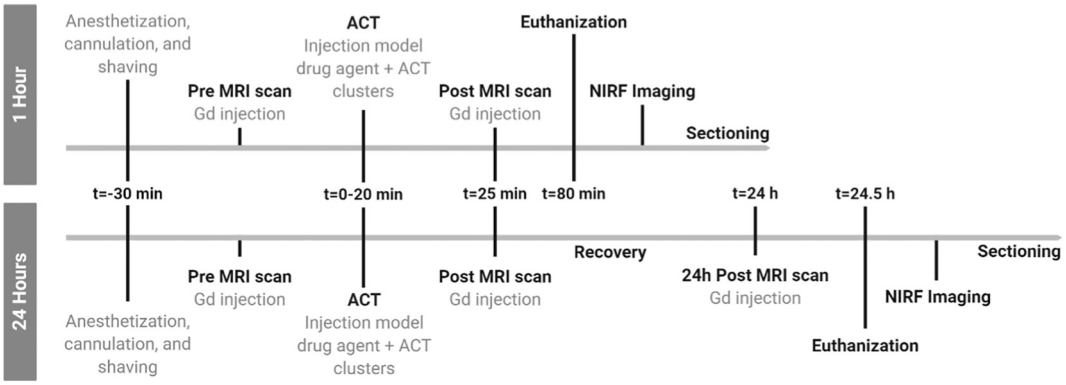

Fig. 2. Timeline for the 1 h and 24 h treatment groups from anesthetization until sectioning of the brains. (Gd = Gadolinium-based contrast agent, ACT® = Acoustic cluster therapy, MRI = Magnetic resonance imaging, NIRF = Near infrared fluorescence).

Table 1
Overview of the treatment groups including a total of 37 animals.

Treatment	Timepoint	Sectioning	Number
Control	1 hour	Fixed	2
		Frozen	6
	24 hours	Fixed	2
		Frozen	6
ACT®	1 hour	Fixed	4
		Frozen	9
	24 hours	Fixed	4
		Frozen	4

IRDye® 800CW-PEG CCPM

Animals received either IRDye® 800CW-PEG (orange) or CCPM (purple) in combination with ACT®. One group of animals were used as controls and received saline instead of ACT®. Euthanization timepoints were 1 h or 24 h post ACT®, after which the brains were either fixed in formalin for HES staining or frozen in liquid nitrogen for CLSM.

animals underwent another MRI-scan (24 h post-MRI scan) the day after ACT®.

The effect of injecting 1 time ACT® and applying only the activation (n = 3), only the enhancement ultrasound (n = 3) or the combined treatment (n = 3) was studied by assessing BBB permeability and accumulation of the IRDye® 800CW-PEG (see supplementary information).

To label the functional vasculature for CLSM, animals received 50 μl of fluorescein (FITC) labelled *Lycopersicon esculentum* tomato lectin (2 mg/ml, Vector Laboratories, UK) 5 min prior to euthanization.

All animals were euthanized by an intraperitoneal injection of pentobarbital (200 μl) and kept under anaesthesia until their breathing halted. Thereafter, they were transcardially perfused with 30 ml of PBS after which the brain was excised and imaged with the NIRF imager.

2.8. Analysis of BBB permeability

To evaluate BBB permeability after ACT®, the gadolinium-induced contrast in T1 images was measured with ImageJ (ImageJ 1.51j, USA). Four regions of interest (ROIs) were drawn around the ventricles (Fig. 3) and their average intensity was obtained at 4–5 consecutive levels (slice thickness 0.4 mm; depth covered 1.6–2.0 mm), all located at eye height. To eliminate any effect of different blood concentrations of the gadolinium contrast agent between pre- and post-MRI scans, the average

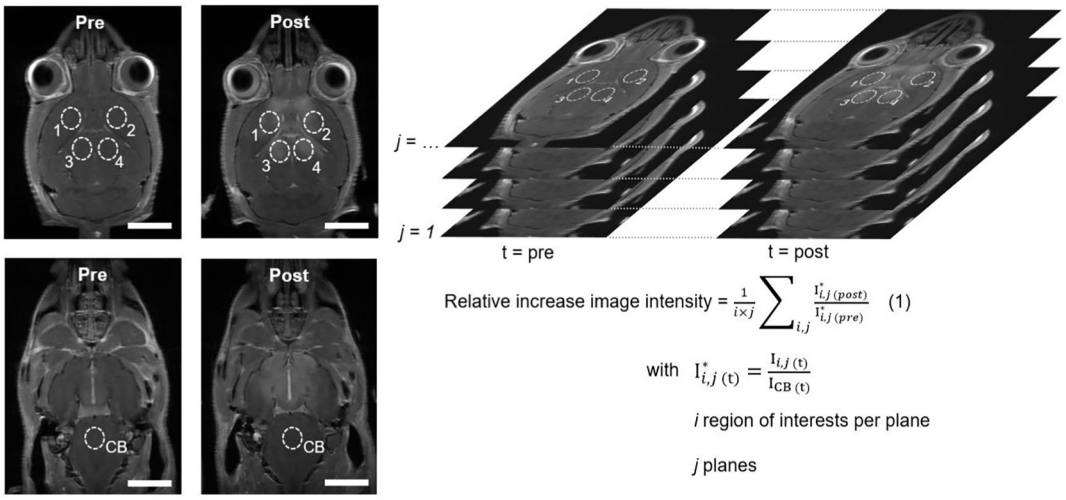

Fig. 3. White circles indicate regions of interest (ROIs). Numbered ROIs represent the area of which the relative increase in image intensity was determined. First, the average intensity of these ROIs was normalized by the average intensity of the ROI labelled CB (cerebellum) at the corresponding timepoint (i.e. pre or post). The normalized intensity of the numbered ROIs was used to calculate the relative increase in image intensity as described by eq. 1. Scalebar represents 4 mm.

intensity of each ROI ($I_{i,j}$) was normalized to the average intensity of an ROI drawn on the cerebellum (I_{CB}). The cerebellum was chosen because of its location outside the ACT®-treated region and its homogenous MR image intensity. Thereafter, the relative increase in intensity with respect to the pre-MRI scan was calculated to evaluate the degree of BBB permeability for each ROI at each level. The average relative increase per animal was calculated by taking the average of all values obtained (see eq. 1). T2 and T1 FLASH images were visually examined to evaluate oedema and haemorrhages, respectively.

2.9. Near infrared fluorescence imaging

Excised brains were placed in a NIRF imager (Pearl Impulse Imager, LI-COR Biosciences Ltd., USA) to assess accumulation of either the IRDye® 800CW-PEG or CCPM in the brain. Fluorophores were excited at 785 nm and fluorescence emission was detected at 820 nm. Images were analysed with ImageJ (ImageJ 1.51j, USA). An ROI was drawn around the brain and the total fluorescence intensity was acquired and normalized to the wet weight of the brain. Standard curves for each of the injected agents (Fig. S1) were used to convert the total fluorescence intensity to the percentage of the injected dose per gram of brain tissue (% ID/g). Results were plotted per timepoint and treatment group.

2.10. Brain sectioning for microscopy

For confocal microscopy, excised brains were mounted transversely on a piece of cork with OCT Tissue Tek (Sakura, The Netherlands) before submerging the sample slowly in liquid nitrogen. Of the frozen brains, the first 500 μm from the top were removed after which 5 × 10 μm thick sections and 5 × 25 μm thick sections were cut transversely. This was repeated every 800 μm throughout the brain.

For histology, excised brains were submerged in formalin for at least 24 h before sectioning. Formalin fixed brains were embedded in paraffin. Thereafter the first 500 μm from the top were removed after which 3 × 4 μm thick sections were cut transversely. This was repeated every 1000 μm throughout the brain. Thereafter sections were stained with HES to evaluate the extent of tissue damage after ACT®.

2.11. Confocal laser scanning microscopy of brain sections

Microdistribution of CCPM was imaged by CLSM using the LSM 800 from Zeiss. Prior to imaging, 25 μm thick frozen brain sections were thawed at room temperature after which they were mounted with Vectashield (Vector Laboratories, USA) and covered with a cover glass. A 20×/0.8 Plan-Apochromat air objective was used to acquire tile scans of the whole section (1024 × 1024 pixels, 16-bit, pixel size 312 nm, 10% overlap between tiles, 2 averages by line). FITC labelled lectin stained blood vessels were imaged by exciting the sections with a 488 nm diode laser and emission was detected between 495 and 540 nm. The Rhodamine B labelled CCPM were excited with a 561 nm diode laser and fluorescence emission was detected between 570 nm and 700 nm. *Z*-stacks at ROI were acquired with a 40×/1.2C-Apochromat water objective (1024 × 1024, 16-bit, pixel size and 321 nm and 156 nm respectively, 0.5 μm increment in z-direction, optical slice thickness 1.0 μm).

CLSM tilescans were analysed with ImageJ (ImageJ 1.51j, USA). The CCPM channel was individually thresholded by built-in threshold function (Li) in ImageJ. Per section, an ROI around the two hemispheres was drawn and the total number of pixels representing CCPM was obtained, normalized to the size of the ROI used and plotted per treatment group. The built-in function 'Analyze particles' from ImageJ was used to obtain information about the size and number of CCPM areas found in each image. The CCPM areas found were divided in three size groups: < 240, 240–24.000 and > 24.000 μm^2. The cut-off values (240 and 24.000) were based on the size of CCPM areas found in the control sections. Approximately 99% of the detected CCPM areas in the control sections had a size below 240 μm^2. The threshold 24.000 μm^2 was based on the average maximal size of CCPM areas found in the six control sections. All CCPM areas with a size above 24.000 μm^2 are referred to as 'clouds'.

2.12. Histology

Tilescans of HES sections were acquired by bright field imaging with the LSM 800 from Zeiss. A 20×/0.8 Plan-Apochromat air objective was used to acquire tilescans of the whole section which were assessed for tissue damage by a senior neuropathologist.

2.13. Statistics

Statistical analysis of all datasets was performed using GraphPad Prism (v8.0, USA). The statistical test used depended on the type and number of datasets compared and is specified in the caption of the corresponding figure. A *p*-value smaller than 0.05 was considered to indicate significance.

3. Results

3.1. Enhanced BBB permeability due to ACT®

Representative T1, T2 and T1 FLASH images are shown in Fig. 4A. An increase in gadolinium-induced contrast caused by extravasation of the gadolinium containing contrast agent due to an enhanced permeability of the BBB, was observed in T1 images taken post ACT®. For all animals, T2 images showed an increased signal intensity colocalizing with the site of BBB disruption, indicating the presence of oedema. In T1-FLASH, besides the gadolinium-induced contrast, a few dark spots were detected.

The relative increase in intensity between pre and post MR images for both the control and ACT®-treated animals are shown in Fig. 4B. The spread of the datapoints in the ACT®-treated group represents the different degrees of BBB permeability obtained. In average, a 1.5-fold increase in gadolinium-induced contrast was observed for animals which received ACT® compared to control animals ($p < 0.001$). 24 h post ACT®, small spots with gadolinium-induced contrast were observed in T1 images (Fig. S2) but disappeared 48 h after, implying recovery of the BBB.

Axial images of a T1 MRI 3D volume demonstrate the extent of gadolinium-induced contrast along the craniocaudal axis (Fig. 4C).

Applying only the activation or enhancement ultrasound resulted in a 1.2-fold and no increase (1-fold) whereas the combined treatment showed a 1.3-fold increase in gadolinium-induced contrast in MR images taken pre and post treatment (Fig. S3).

3.2. Increased accumulation of the IRDye® 800CW-PEG and CCPM after ACT®

MRI showed clear extravasation of the gadolinium-containing contrast agent indicating increased permeability of the BBB after ACT®. To study whether the increased permeability would facilitate extravasation of IRDye® 800CW-PEG (25–60 kDa) and CCPM (65 nm), excised brains were imaged in a NIRF imager. Representative NIRF-images of animals injected with the macromolecule and CCPM are shown in Fig. 5A and B, respectively.

For both agents, increased accumulation could be observed in brains which received ACT® compared to the control brains. Quantitative analysis of the NIRF-images revealed a statistically significant increase in accumulation (% ID/g) between the ACT® and control animals for both agents and at both timepoints (Fig. 5C-D). For animals injected with the IRDye® 800CW-PEG, the average % ID/g increased from 1.1 ±

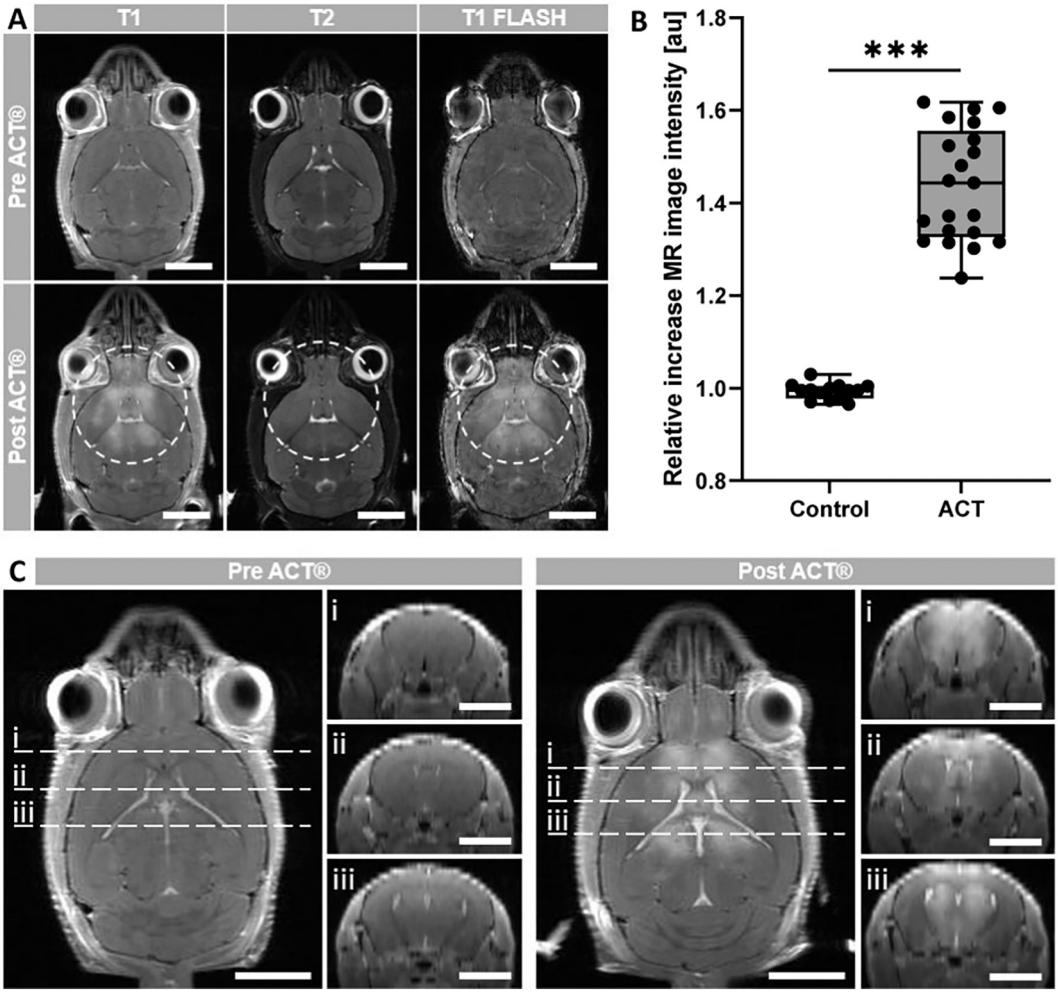

Fig. 4. (A) Representative T1, T2 and T1 FLASH images of animals pre and post ACT®. Dashed white circles indicate the area treated with ACT®. A clear signal intensity increase can be observed in the T1 and T1 FLASH images taken post ACT®. The observed signal intensity in the T2 images colocalizes with the site of increased BBB permeability and indicates the presence of oedema. (B) Relative increase in MR image intensity between T1 images acquired pre and post treatment for control ($n = 14$) and ACT®-treated animals ($n = 21$). Asterisks show statistical significance (***$p < 0.001$). *P*-values were derived from a student's *t*-test. (C) Coronal and corresponding (i-iii) axial images of a T1 3D MR image volume acquired pre (left panel) and post ACT® (right panel). In the post ACT® MR images, gadolinium-induced contrast can be observed around the ventrical system and along the craniocaudal axis. In all images, scalebar represents 4 mm.

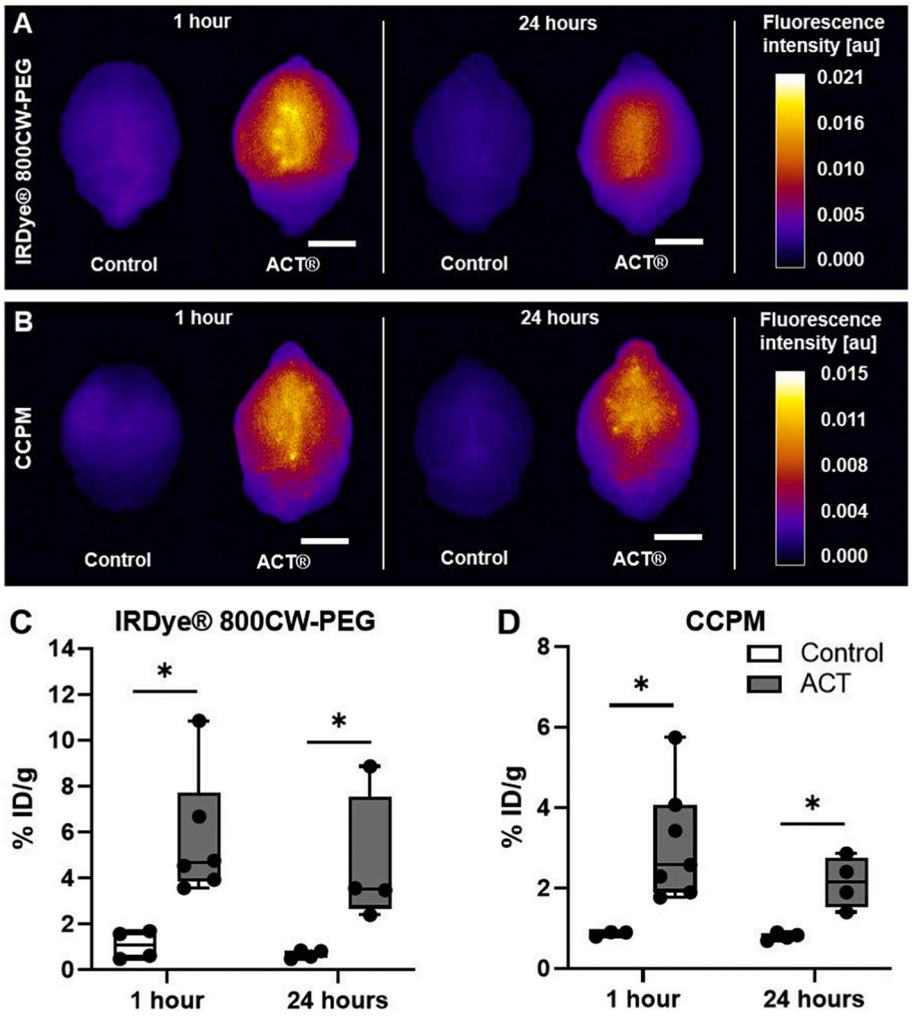

Fig. 5. Representative NIRF-images of excised brains of animals injected with (A) IRDye® 800CW-PEG or (B) CCPM. ACT®-treated brains showed increased accumulation opposed to control brains for both injected agents at 1 h and 24 h post ACT®. Scalebar represents 4 mm. The % ID/g for animals injected with (C) the IRDye® 800CW-PEG and (D) CCPM verifies the observed differences and shows a statistically significant difference between the control (white) and ACT®-treated (grey) animals for each injectable at both timepoints. Asterisk shows statistical significance. (*$p < 0.05$) *P*-values were derived from a Mann-Whitney Rank sum test. Boxplot based on $n = 4$–7 animals. (% ID/g indicates percentage of injected dose per gram of brain tissue).

0.5% ID/g in the control animals to 5.7 ± 2.5% ID/g in ACT®-treated animals 1 h after ACT®. At 24 h after injection, 0.7 ± 0.2% ID/g was observed for the controls and 4.6 ± 2.5% ID/g in the ACT®-treated animals. Hence, ACT® induced a 5.2-fold and 6.6-fold increase in % ID/g in the 1 h and 24 h treatment group, respectively. For animals injected with CCPM, the average % ID/g increased from 0.9 ± 0.1% ID/g to 3.3 ± 1.3% ID/g at 1 h, and from 0.8 ± 0.1% ID/g to 2.1 ± 0.5% ID/g 24 h after treatment. Respectively, a 3.7-fold and 2.6-fold increase in % ID/g was observed. No statistically significant difference was found between both timepoints neither for IRDye® 800CW-PEG nor CCPM, indicating that the agents are retained in the extravascular space for 24 h.

Corresponding NIRF images of animals receiving 1 time ACT® showed in average a 2.2-fold increase in % ID/g. Only activation exposure resulted in a 1.7-fold increase in % ID/g while only enhancement exposure yielded no increase in brain accumulation (Fig. S3).

3.3. Extravasation of CCPM observed in ACT®-treated brains

To verify that the increased accumulation of the CCPM in brain tissue after ACT® was due to extravasation of the CCPM, the location of CCPM with respect to blood vessels, was imaged on frozen brain sections by CLSM. Tilescans of ACT®-treated brains showed several 'clouds' of fluorescence which were not observed in brains of control animals (Fig. 6). Depending on which section level in the brain was imaged, CCPM were more profoundly present in the cerebral cortex (Fig. S4). Tilescans of the 24 h treatment group showed similar cloud patterns as the 1 h treatment group (Fig. S5). From thresholded tilescans of both control and ACT®-treated animals, the number of pixels representing CCPM were extracted and normalized to the size of the ROI used to outline the hemispheres. A statistically significant 4.7-fold increase can be observed in the 1 h post ACT®-treated sections as opposed to the control brains (Fig. 7) which is a larger increase than observed in the NIRF images. From the thresholded CCPM image, individual areas with CCPM could be identified and their size was analysed (Table 2). From Table 2 it can be seen that the large CCPM areas (>24.000, 'clouds') observed in the ACT®-treated brains accounted for approximately 55% of the pixels representing CCPM. In average, 17 of these clouds were observed per ACT®-treated brain section whereas only 1 was observed per control section.

High magnification CLSM images at different locations in both the control brains and the ACT®-treated brains were acquired to study the location of the CCPM with respect to the blood vessels (Fig. 6, i-iv). In ACT®-treated brains, CCPM had extravasated and penetrated into the brain parenchyma whereas in control brains CCPM were mainly observed intravascularly or minimally displaced from the blood vessel staining. 3D renderings of acquired CLSM *Z*-stacks showed this more clearly (Fig. S6).

3.4. No haemorrhages observed in HES stained sections of brains after ACT®

Representative T1 FLASH MR images and corresponding HES stained sections of ACT®-treated brains 1 h and 24 h post ACT® are shown in Fig. 8. MR images showed a few dark spots which could represent

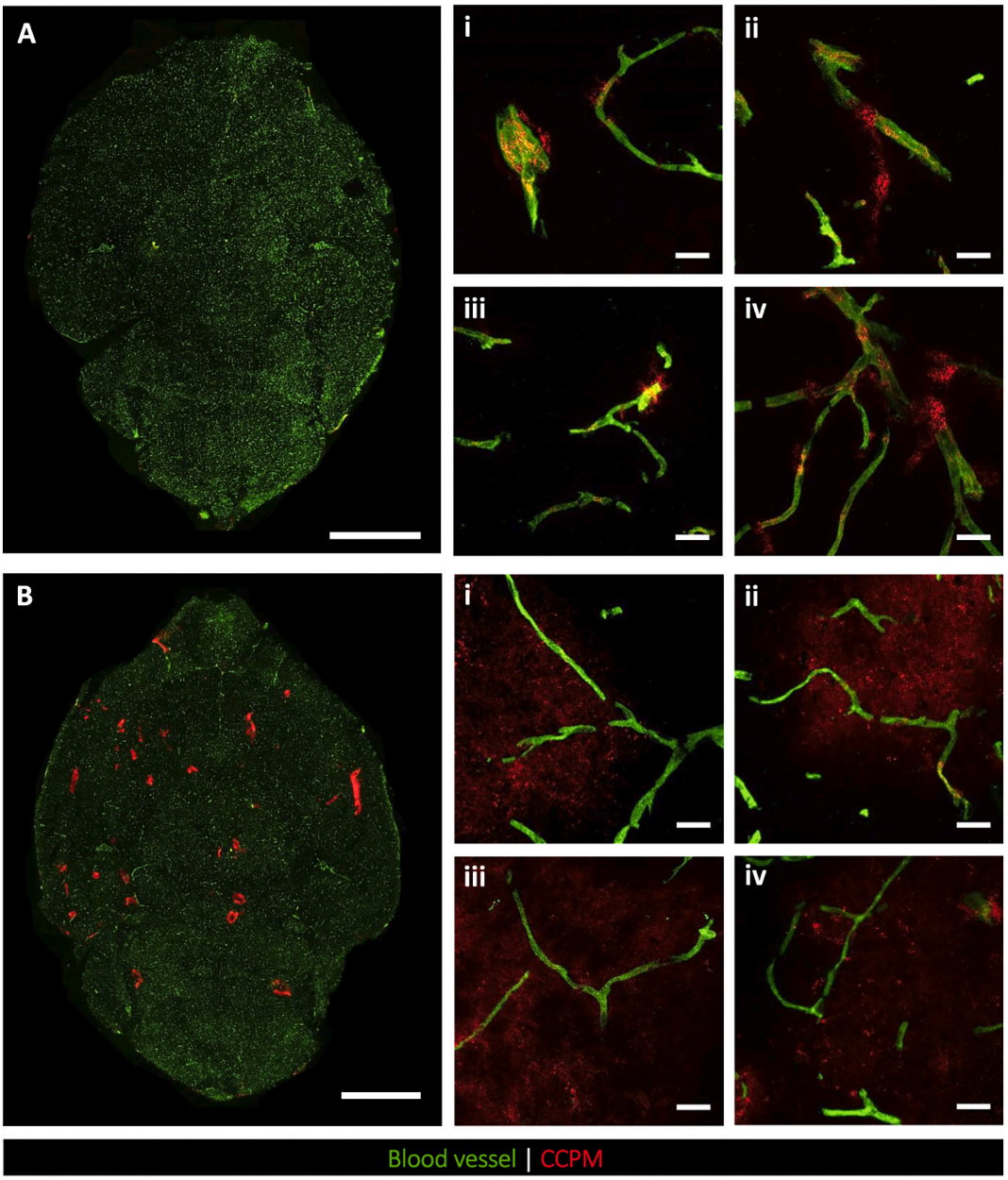

Fig. 6. CLSM tilescans acquired with a 20×/0.8 air objective of (A) a control brain and (B) an ACT®-treated brain of animals euthanized 1 h post ACT®. Blood vessels are shown in green and CCPM in red. (i-iv) Selection of acquired Z-projection (sum of slices) of CLSM Z-stack images acquired with a 40×/1.2 water objective. Scalebar in tilescans and zoom-ins represents 2000 μm and 20 μm, respectively. (For interpretation of the references to colour in this figure legend, the reader is referred to the web version of this article.)

haemorrhages, dilated vessels or undissolved gas. High magnification images of HES stained sections revealed a few spots with extravasated erythrocytes (Fig. 8 C,F) that were of no clinical relevance. In Fig. 8 C extravasated erythrocytes accumulated in an embryonical area populated by primitive neurons. No haemorrhages, infiltrating neutrophils or damaged endothelial cells or neurons could be detected.

4. Discussion

This work demonstrated that ACT® can increase the permeability of the BBB in a temporal and safe fashion and improve transport of co-administered compounds into the brain, whose passage is normally impaired by the BBB. Next to the small hydrophilic macromolecule IRDye® 800CW-PEG, the larger clinically relevant CCPM nanocarriers showed enhanced accumulation and penetration in the murine brain post ACT®. These findings generate new treatment options for a range of neurological applications that would benefit from a combined therapy.

ACT®-induced increase of the BBB permeability was evaluated by contrast-enhanced MR imaging and confirmed by the observed increased accumulation of the IRDye® 800CW-PEG and CCPM in NIRF images of excised brains. Integrity changes of the BBB are expected to be caused by the combined effect of the activation and enhancement ultrasound exposure steps of the ACT® concept. The rapid vaporization (μs) of microdroplets into larger microbubbles, may cause a pressure-induced temporary stretch of brain capillaries (3–4 μm) [33]. The vasodilation might activate mechanosensitive intracellular pathways as well as alter the inter-endothelial tight junctions, allowing co-injected agents to extravasate [34]. The subsequent enhancement step will cause the large activated ACT® bubbles to oscillate, inducing pressure waves on the blood vessel wall, which may enhance para- and trans-

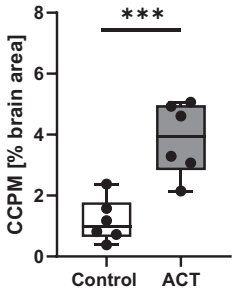

Fig. 7. The number of pixels representing CCPM presented as the percentage of the size of brain area analysed for both the control and ACT®-treated animals ($n = 6$). Per group, two brain levels in three animals were imaged. *P*-values were derived with a *t*-test. (***$p < 0.001$).

Table 2
Analysis of the CCPM areas observed in CLSM tilescans of control (CTRL) and ACT®-treated animals (ACT®).

Size CCPM area [μm^2]		Average size [μm^2]	Number	% of total number of CCPM pixels
<240	CTRL	48 ± 4	7225 ± 3804	48.7 ± 12.3
	ACT®	44 ± 10	10,067 ± 5648	18.1 ± 9.2**
240–24.000	CTRL	774 ± 218	469 ± 299	47.4 ± 9.0
	ACT®	1208 ± 428	750 ± 623	26.4 ± 9.8**
>24.000	CTRL	350,537 ± 6699	1 ± 1	3.9 ± 4.8
	ACT®	80,863 ± 18541**	17 ± 5***	55.5 ± 18.3**

The average size, number of areas and percentage of the total number of CCPM pixels the CCPM areas account for in the CLSM tilescans. *t*-tests were employed to test for statistically significance between the control and ACT®-treated group. (n = 6 per group) (*$p < 0.05$, **$p < 0.01$, ***p < 0.001).

endothelial transport of the co-injected agents. Applying only the activation ultrasound resulted in a modest gadolinium-enhanced contrast and accumulation of IRDye® 800CW-PEG, while applying only the enhancement ultrasound did not increase the permeability of the BBB and accumulation of the IRDye® 800CW-PEG. This is in line with the expected mechanism of ACT®. The low ultrasound frequency and low pressures of the enhancement step are sub-optimal for the ACT® clusters, neither activating them, nor causing them to oscillate sufficiently to facilitate extravasation of the co-injected agents. Although ACT® bubbles seem to induce structural changes to the BBB, there is no evidence of relevant tissue disruption. No cellular responses, such as degenerative changes in neurons, endothelial damage or infiltration of neutrophils, indicating an inflammatory response to the treatment could be observed from HES stained sections. T1 FLASH MR images showed a few dark spots which potentially could represent haemorrhages. However, histological investigation only showed a few extravasated erythrocytes but no haemorrhages, indicating that ACT® did not provoke substantial damage. Thus, the dark spots observed in the T1 FLASH MR images probably represent other ACT®-induced effects such as dilated vessels.

Upon ACT®, a spotted pattern of gadolinium enhanced contrast in MR images was observed in the brain which is in line with previous work utilizing ACT® [24] despite the differences in experimental parameters. The spotted pattern may be caused by the small fraction of injected ACT® clusters that will be activated resulting in only a limited number of ACT® bubbles lodging in the vasculature of the targeted tissue. Additionally, the lodged ACT® bubbles will vary in size and shape depending on the type of vessel they are residing in such that they will respond heterogeneously to the enhancement ultrasound [16,17]. The activation yield and bubble oscillations may be further affected by the distorted ultrasound beam profile caused by the curvature and varying thickness of the skull.

The enhanced BBB permeability was still clearly observed 24 h post ACT® treatment but 48 h after treatment, no gadolinium-enhanced contrast was observed in the MR images, indicating recovery of the BBB. The observed recovery time is in the same range as what others have reported [35–37], and similar to what has been observed previously with ACT® [24]. Temporary and localized disruption of the BBB was obtained using lower acoustic pressures (0.2–0.4 MPa and 0.08–0.12 MPa) than reported in studies using conventional microbubbles (0.3–0.6 MPa) [37] and beneath the reported threshold value for damage [11].

For both the IRDye® 800CW-PEG and CCPM, a significant increase in accumulation was observed in ACT®-treated brains compared to control brains. Accumulation was highest 1 h after ACT® but did not differ significantly from 24 h post ACT®. This indicates that both compounds were able to retain in the parenchyma for 24 h post ACT®. Microvascular changes induced by ACT® could have affected the brain interstitial fluid flow thereby impairing brain clearance [38]. Accumulation of the IRDye® 800CW-PEG macromolecule (45 kDa) was approximately 2 times higher compared to CCPM (65 nm). A superior accumulation of the macromolecule over CCPM was expected, since smaller sized compounds have been observed to extravasate more efficiently across the BBB after ultrasound-induced increase of the BBB permeability compared to larger compounds [39,40].

In CLSM tile scans of ACT®-treated brain sections, CCPM appeared in clouds distributed throughout the brain whereas no clouds were observed in control sections. The area in which clouds were observed exceeded the −3 dB activation ultrasound beam width (Ø 6 mm), which is most likely a result of activated ACT® bubbles circulating through the vasculature before lodging in smaller capillaries. An average of 17 clouds were observed per ACT®-treated brain and individual clouds could be a result of one large ACT® bubble, a fusion of smaller ACT® bubbles or several smaller ACT® bubbles generating overlapping extravasation sites.

High magnification CLSM images of control brains revealed that CCPM were observed both intra- and extravascular. In case of the former, CCPM were most likely adsorbed to the brain endothelium via non-specific binding since brains were perfused before being excised. CCPM observed extravascular were only minimal displaced with respect to the stained blood vessels. In these cases, extravascular CCPM were expected to be located mainly in either endothelial cells or the perivascular space. However, this nanoparticle-mediated transport would result in inadequate drug delivery to the brain and thus not be of clinical relevance [41]. High magnification CLSM images of ACT®-treated brains showed that ACT® did not only increase the permeability of the BBB enabling CCPM to extravasate, but also caused the CCPM to displace from the capillaries and penetrate further into the brain parenchyma. The mechanism of ultrasound and microbubble induced penetration of nanoparticles into extracellular space is not fully understood. For regular ultrasound contrast agents, microstreaming, acoustic streaming and/or oscillating microbubbles affecting the perivascular pumping effect induced by arterial pulsion are suggested to effect penetration depth [42–44]. The polydisperse ACT® bubbles may create heterogenous microstreaming patterns and perivascular pumping effects, and therefore may change the permeability of the BBB to different degrees. After ACT®-induced changes in the BBB permeability, the successful extravasation and penetration of CCPM into the brain parenchyma can also be attributed to properties of the CCPM such as the lack of protein corona after systemic administration resulting in a long circulation half-life (16 h in rats) [32,45].

5. Conclusion

The results indicate that ACT® safely increased the permeability of the BBB using acoustic pressures in the diagnostic range and improved extravasation and penetration of co-administered compounds into the

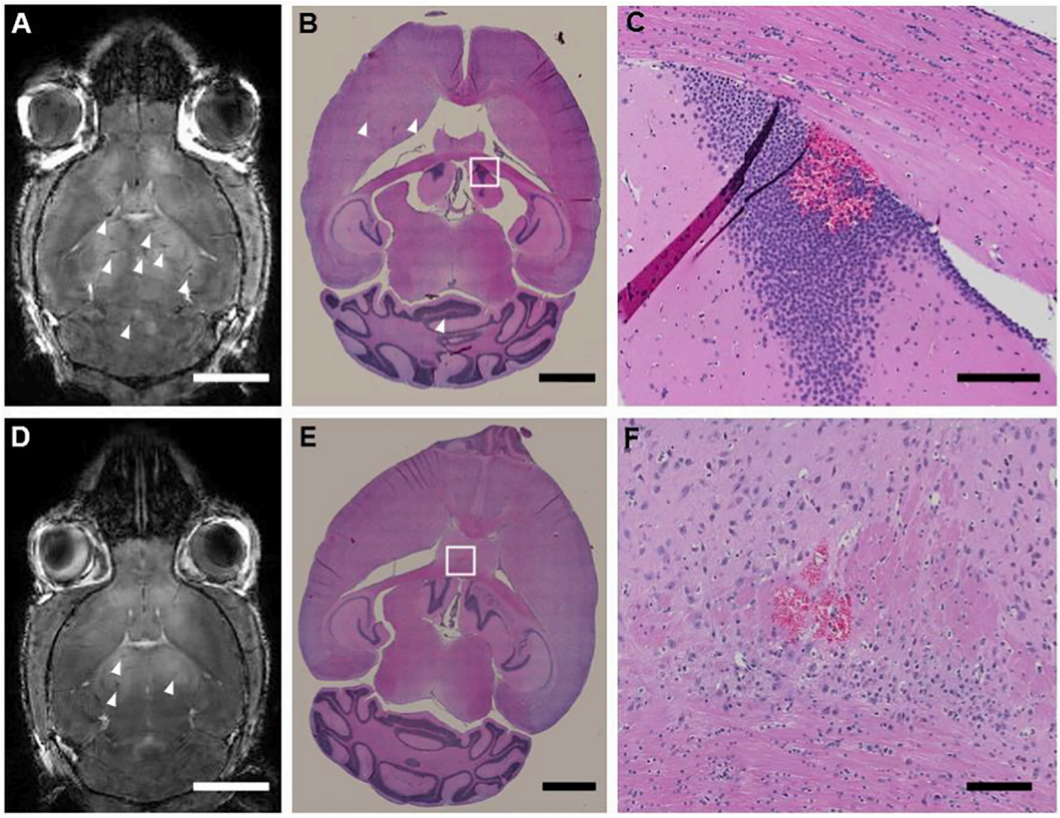

Fig. 8. Histological analysis of representative brains of animals euthanized 1 h (upper panel) and 24 h post ACT® (lower panel). (A,D) Post ACT® T1 FLASH MRI image. White arrows indicate potential locations of haemorrhages. Scalebar is 4000 μm. (B,E) Tilescans of corresponding HES stained brain sections. White arrows indicate areas with extravasation of erythrocytes. Scalebar is 2000 μm. (C,F) High magnification images of ROIs drawn in B and E, respectively, showing more clearly the extravasation of erythrocytes. Scalebar is 200 μm.

brain parenchyma. Increased brain accumulation of the clinically relevant and versatile CCPM upon ACT® is a promising strategy for treating brain disorders such as neurodegenerative dementias and structural pathologies such as malignant brain tumours.

Declaration of interest

Marieke Olsman, Melina Mühlenpfordt, Emma Bøe Olsen, Sverre H. Thorp, Sofie Snipstad and Catharina de Lange Davies declare no competing interests. Qizhi Hu, Cristianne J.F. Rijcken and Marielle Thewissen are all employees of Cristal Therapeutics; Cristianne Rijcken is also shareholder of Cristal Therapeutics. Spiros Kotopoulis is currently employed and is a shareholder of EXACT Therapeutics, an ultrasound and microbubble enhanced therapy company.

Acknowledgements

Housing of animals was provided by the Comparative Medicine Core Facility (CoMed, NTNU). MR imaging was performed at the MR Core Facility (NTNU) and Deborah Hill and Marius Widerøe are thanked for their technical support. Tissue sections were prepared by the Cellular and Molecular Imaging Core facility (CMIC, NTNU). CLSM was performed at the Centre for Advanced Microscopy at the Faculty of Natural Sciences (CAM, NTNU). Illustrations were created with BioRender.com. The project was funded by the Norwegian University of Science and Technology (NTNU, Trondheim, Norway) and the Research Council of Norway Nano2021 262228.

Appendix A. Supplementary data

Supplementary data to this article can be found online at https://doi.org/10.1016/j.jconrel.2021.07.019.

References

[1] N.J. Abbott, et al., Structure and function of the blood-brain barrier, Neurobiol. Dis. 37 (1) (2010) 13–25.
[2] W.M. Pardridge, Drug transport across the blood-brain barrier, J. Cereb. Blood Flow Metab. 32 (11) (2012) 1959–1972.
[3] S.V. Dhuria, L.R. Hanson, W.H. Frey 2nd, Intranasal delivery to the central nervous system: mechanisms and experimental considerations, J. Pharm. Sci. 99 (4) (2010) 1654–1673.
[4] J.J. Lochhead, R.G. Thorne, Intranasal delivery of biologics to the central nervous system, Adv. Drug Deliv. Rev. 64 (7) (2012) 614–628.
[5] S.I. Rapoport, Osmotic opening of the blood-brain barrier: principles, mechanism, and therapeutic applications, Cell. Mol. Neurobiol. 20 (2) (2000) 217–230.
[6] E. White, et al., A robust MRI-compatible system to facilitate highly accurate stereotactic administration of therapeutic agents to targets within the brain of a large animal model, J. Neurosci. Methods 195 (1) (2011) 78–87.
[7] A. Burgess, et al., Focused ultrasound-mediated drug delivery through the blood-brain barrier, Expert. Rev. Neurother. 15 (5) (2015) 477–491.
[8] A. Burgess, K. Hynynen, Noninvasive and targeted drug delivery to the brain using focused ultrasound, ACS Chem. Neurosci. 4 (4) (2013) 519–526.
[9] K. Hynynen, et al., Noninvasive MR imaging-guided focal opening of the blood-brain barrier in rabbits, Radiology 220 (3) (2001) 640–646.
[10] H.L. Liu, et al., Combining microbubbles and ultrasound for drug delivery to brain tumors: current progress and overview, Theranostics 4 (4) (2014) 432–444.
[11] N. McDannold, N. Vykhodtseva, K. Hynynen, Blood-brain barrier disruption induced by focused ultrasound and circulating preformed microbubbles appears to be characterized by the mechanical index, Ultrasound Med. Biol. 34 (5) (2008) 834–840.
[12] N. McDannold, N. Vykhodtseva, K. Hynynen, Effects of acoustic parameters and ultrasound contrast agent dose on focused-ultrasound induced blood-brain barrier disruption, Ultrasound Med. Biol. 34 (6) (2008) 930–937.
[13] S. Meairs, A. Alonso, Ultrasound, microbubbles and the blood-brain barrier, Prog. Biophys. Mol. Biol. 93 (1–3) (2007) 354–362.
[14] C. Poon, D. McMahon, K. Hynynen, Noninvasive and targeted delivery of therapeutics to the brain using focused ultrasound, Neuropharmacology 120 (2016) 20–37.

[15] C.Y. Ting, et al., Concurrent blood-brain barrier opening and local drug delivery using drug-carrying microbubbles and focused ultrasound for brain glioma treatment, Biomaterials 33 (2) (2012) 704–712.
[16] P. Sontum, et al., Acoustic cluster therapy (ACT)–a novel concept for ultrasound mediated, targeted drug delivery, Int. J. Pharm. 495 (2) (2015) 1019–1027.
[17] A.J. Healey, et al., Acoustic cluster therapy: in vitro and ex vivo measurement of activated bubble size distribution and temporal dynamics, Ultrasound Med. Biol. 42 (5) (2016) 1145–1166.
[18] A. van Wamel, et al., Acoustic cluster therapy (ACT)—pre-clinical proof of principle for local drug delivery and enhanced uptake, J. Control. Release 224 (2016) 158–164.
[19] O. Myhre, et al., Safety assessment in rats and dogs of Acoustic Cluster Therapy, a novel concept for ultrasound mediated, targeted drug delivery, Pharmacol. Res. Perspect. (2016) 4(6).
[20] A. van Wamel, et al., Acoustic cluster therapy (ACT) enhances the therapeutic efficacy of paclitaxel and Abraxane® for treatment of human prostate adenocarcinoma in mice, J. Control. Release 236 (2016) 15–21.
[21] S. Kotopoulis, et al., Sonoporation with acoustic cluster therapy (ACT®) induces transient tumour volume reduction in a subcutaneous xenograft model of pancreatic ductal adenocarcinoma, J. Control. Release 245 (2017) 70–80.
[22] N. Bush, et al., Theranostic attributes of acoustic cluster therapy and its use for enhancing the effectiveness of liposomal doxorubicin treatment of human triple negative breast cancer in mice, Front. Pharmacol. 11 (2020) 75.
[23] N.L. Bush, et al., Therapeutic dose response of acoustic cluster therapy in combination with irinotecan for the treatment of human colon cancer in mice, Front. Pharmacol. 10 (2019) 1299.
[24] A.K. Åslund, et al., Efficient enhancement of blood-brain barrier permeability using acoustic cluster therapy (ACT), Theranostics 7 (1) (2017) 23.
[25] M. Talelli, et al., Core-crosslinked polymeric micelles: principles, preparation, biomedical applications and clinical translation, Nano Today 10 (1) (2015) 93–117.
[26] Q. Hu, et al., Tailoring the physicochemical properties of core-crosslinked polymeric micelles for pharmaceutical applications, J. Control. Release 244 (2016) 314–325.
[27] M. Coimbra, et al., Antitumor efficacy of dexamethasone-loaded core-crosslinked polymeric micelles, J. Control. Release 163 (3) (2012) 361–367.
[28] Q. Hu, et al., Complete regression of breast tumour with a single dose of docetaxel-entrapped core-cross-linked polymeric micelles, Biomaterials 53 (2015) 370–378.
[29] F. Atrafi, et al., A phase I dose-escalation and pharmacokinetic study of a micellar nanoparticle with entrapped docetaxel (CPC634) in patients with advanced solid tumours, J. Control. Release 325 (2020) 191–197.
[30] K.K. Andersen, et al., A harmonic dual-frequency transducer for acoustic cluster therapy, Ultrasound Med. Biol. 45 (9) (2019) 2381–2390.
[31] H.-A. Klok, et al., Cholesteryl-(L-lactic acid) n building blocks for self-assembling biomaterials, Macromolecules 35 (3) (2002) 746–759.
[32] I. Biancacci, et al., Optical imaging of the whole-body to cellular biodistribution of clinical-stage PEG-b-pHPMA-based core-crosslinked polymeric micelles, J. Control. Release 328 (2020) 805–816.
[33] P.S. Tsai, et al., Correlations of neuronal and microvascular densities in murine cortex revealed by direct counting and colocalization of nuclei and vessels, J. Neurosci. 29 (46) (2009) 14553–14570.
[34] M. Anwar, et al., The effect of pressure-induced mechanical stretch on vascular wall differential gene expression, J. Vasc. Res. 49 (6) (2012) 463–478.
[35] A.K. Åslund, et al., Nanoparticle delivery to the brain—by focused ultrasound and self-assembled nanoparticle-stabilized microbubbles, J. Control. Release 220 (2015) 287–294.
[36] S. Wang, et al., Microbubble type and distribution dependence of focused ultrasound-induced blood–brain barrier opening, Ultrasound Med. Biol. 40 (1) (2014) 130–137.
[37] G. Samiotaki, E.E. Konofagou, Dependence of the reversibility of focused-ultrasound-induced blood-brain barrier opening on pressure and pulse length in vivo, IEEE Trans. Ultrason. Ferroelectr. Freq. Control 60 (11) (2013) 2257–2265.
[38] N.J. Abbott, Evidence for bulk flow of brain interstitial fluid: significance for physiology and pathology, Neurochem. Int. 45 (4) (2004) 545–552.
[39] S. Ohta, et al., Investigating the optimum size of nanoparticles for their delivery into the brain assisted by focused ultrasound-induced blood–brain barrier opening, Sci. Rep. 10 (1) (2020) 1–13.
[40] B. Marty, et al., Dynamic study of blood–brain barrier closure after its disruption using ultrasound: a quantitative analysis, J. Cereb. Blood Flow Metab. 32 (10) (2012) 1948–1958.
[41] J. Kreuter, Drug delivery to the central nervous system by polymeric nanoparticles: what do we know? Adv. Drug Deliv. Rev. 71 (2014) 2–14.
[42] P. Hadaczek, et al., The "perivascular pump" driven by arterial pulsation is a powerful mechanism for the distribution of therapeutic molecules within the brain, Mol. Ther. 14 (1) (2006) 69–78.
[43] H. Chen, et al., Focused ultrasound-enhanced intranasal brain delivery of brain-derived neurotrophic factor, Sci. Rep. 6 (2016) 28599.
[44] M. Afadzi, et al., *Effect of Acoustic Radiation Force on the Distribution of Nanoparticles in Solid Tumors.* IEEE Transactions on Ultrasonics, Ferroelectrics, and Frequency Control, 2020.
[45] Q. Hu, et al., High systemic availability of core-crosslinked polymeric micelles after subcutaneous administration, Int. J. Pharm. 514 (1) (2016) 112–120.